# Highlights

## Identification of distinct flow behaviours around twin rough cylinders at low wind incidence

Raphaël Dubois,Thomas Andrianne

- The flow around two static rough cylinders is investigated in the sub- and post-critical regimes.
- The spacing ratio is set to $L/D = 1.2$ and the wind incidence is varied between 0° and 10°.
- Unsteady pressure distributions are measured on the surface of the two cylinders.
- An original method based on the analysis of the unsteady pressure field in the frequency domain is presented.
- Distinct flow behaviours are identified, depending on the wind incidence and the flow regime.
- Eddy shedding is identified in the range $0.14 < St < 0.25$ for all tested configurations.

# Identification of distinct flow behaviours around twin rough cylinders at low wind incidence

Raphaël Dubois[a,*], Thomas Andrianne[a]

[a]Department of Aerospace and Mechanical Engineering, University of Liège, Allée de la Découverte 9, 4000 Liège, Belgium

## ARTICLE INFO

*Keywords*:
Twin circular cylinders
Wind tunnel
Wind incidence
Gap flow
Bi-stability

## ABSTRACT

Wind tunnel experiments are performed on twin rough cylinders with a centre-to-centre spacing ratio $L/D = 1.2$. The unsteady flow field is measured at two different Reynolds numbers, Re = 45k and 275k, corresponding to the sub- and post-critical flow regimes, respectively. The wind incidence $\alpha$ is varied from 0° to 10°. The detailed analysis of the lift coefficients as a function of the wind incidence reveals the existence of three flow behaviours in both flow regimes. Bi-stabilities are observed and occur within different ranges of wind incidence depending on the flow regime. A methodology is proposed to decouple the modes which intermittently occur in case of bi-stability, allowing to identify the flow behaviour of each mode. In the sub-critical flow regime, the flow behaviour at very low wind incidences ($\alpha = 0°$-$2°$) corresponds to an alternate re-attachment on both sides of the rear cylinder. In the post-critical flow regime, the flow behaviour is bi-stable because of the intermittent re-attachment of the shear layers. For larger wind incidences ($\alpha = 4°$-$6°$), the lower shear layer intermittently re-attaches steadily or alternately onto the rear cylinder in the sub-critical flow regime, evidencing a bi-stability. On the other hand, it always re-attaches steadily onto the rear cylinder in the post-critical flow regime. A gap flow is observed for the largest wind incidences ($\alpha = 8°$-$10°$). It is found to be stronger in the sub- than in the post-critical flow regime.

## 1. Introduction

Cylinder-like structures can be found in various engineering applications such as heat exchangers, chimneys, cables, buildings, offshore structures, struts, landing gears, etc. In many cases, air- or water-flows occur around these single or multiple circular cylinder(s) and may eventually lead to fluid-structure interactions. A thorough understanding of the flow is therefore essential at the design stage of such structures. For this reason, fluid flows around circular cylinder have been extensively studied in the past. Several comprehensive reviews of the flow around a single, isolated circular cylinder exist in the literature and are summarised in Zdravkovich (1997). In some applications, the structure consists in twin cylinders. The flow around two cylinders placed in proximity has been investigated to a lesser extent than a single cylinder but has already been the subject of several studies. The two circular cylinders can be placed in various arrangements. The present investigation focuses on the staggered configuration (shown in Fig. 1) which corresponds to the most general arrangement of two parallel circular cylinders with equal diameter in a cross-flow. Tandem and side-by-side configurations have been respectively studied by Igarashi (1981) and Bearman and Wadcock (1973), among others. Researchers also investigated the flow around non-parallel tandem cylinders (e.g. Younis, Alam and Zhou (2016) and Alam, Rastan, Wang and Zhou (2022)), revealing a strong spanwise flow interaction, or around tandem cylinders with different diameters (e.g. Igarashi (1982) and Wang, Alam and Zhou (2018)).

Zdravkovich (1987) classified the flow interference between two parallel circular cylinders into four particular kinds: (i) proximity interference, when the cylinders are close to each other but none of them is found in the wake of another (e.g. side-by-side configuration); (ii) wake interference, when the rear cylinder is near to or submerged into the wake of the front cylinder and the flow around the latter is unaffected by the presence of the other cylinder; (iii) proximity and wake interference, when a combination of both proximity and wake interferences occurs; (iv) no interference, when the interference is considered negligible. Sumner, Price and Païdoussis (2000) identified nine different flow patterns depending on the centre-to-centre spacing ratio $L/D$ and wind incidence $\alpha$ by means of flow visualisation. This large number of flow patterns reveals the complexity of the flow. Alam, Sakamoto and Zhou (2005) measured the unsteady

---

*Corresponding author.
raphael.dubois@uliege.be (R. Dubois)
ORCID(s): 0000-0002-7539-8362 (R. Dubois)

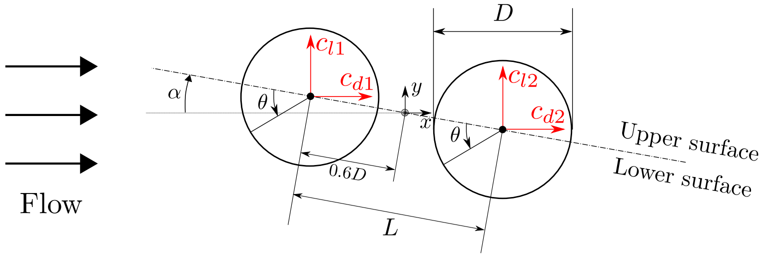

**Figure 1:** Staggered configuration of twin circular cylinders in cross-flow.

forces and pressures acting on twin cylinders for different wind incidences and spacing ratios. The flow behaviours were identified using surface-oil visualisations. For some arrangements (e.g. $L/D = 1.1$ and $\alpha = 10°$), a bi-stability of the flow was observed.

Circular-shaped bodies exhibit a strong Reynolds number dependency, leading to different flow regimes. Zhou, Feng, Alam and Bai (2009) investigated the effect of the Reynolds number on the Strouhal number of staggered cylinders, but their work is limited to the sub-critical flow regime. In the same regime, Igarashi (1981) and more recently Alam (2014) classified the flow patterns around tandem cylinders as a function of the Reynolds number and spacing ratio. Sumner (2010) reviewed the works on two circular cylinders in a cross-flow. He showed that most of the previous studies on staggered cylinders have been performed in the sub-critical flow regime. The question then arises as to what happens at different flow regimes, i.e. in the super- and post-critical regimes. Sun, Gu, He and Zhang (1992) examined the fluctuating pressure on staggered cylinders in the super-critical flow regime. Schewe and Jacobs (2019) investigated the flow around twin smooth cylinders from sub- to post-critical flow regimes in a high-pressure wind tunnel. The experiments consisted in time-averaged aerodynamic force measurements. The resulting force coefficient curves reveal hysteresis behaviours. Although the set-up was meant to be static, vibration issues were reported in the post-critical flow regime. Therefore, the authors supported the need to measure unsteady quantities to better understand the potential flow-induced vibrations.

The present study consists in wind tunnel measurements of the unsteady flow field around two staggered cylinders. The experimental tests are performed at two different Reynolds numbers which correspond to the sub- and post-critical flow regimes, respectively. Similarly to Okajima (1979) and Dubois and Andrianne (2022) for tandem cylinders, adapted surface roughness is applied on the cylinders to reach the post-critical flow regime at lower Reynolds numbers. The centre-to-centre spacing ratio is set to $L/D = 1.2$ and the wind incidence is varied between 0° and 10°. This closely spaced and slightly staggered configuration implies that the resulting flow behaviours all belong to the third kind of interference defined by Zdravkovich (1987), i.e. proximity and wake interference. It should be pointed out that the flow is strongly dependent on the spacing ratio and that the present results are therefore valid for the particular value of $L/D = 1.2$. The lift coefficients are first analysed, revealing the occurrence of bi-stabilities or a strong gap flow between the cylinders. A methodology to decouple the stable states/modes is presented in case of bi-stability. The gap flow is finally analysed by means of time-averaged pressure distributions in the sub- and post-critical flow regimes. This procedure is applicable to any twin configurations which might exhibit different flow behaviours.

## 2. Experimental set-up

The experiments are conducted in the facility of the University of Liège which consists in a closed-loop low-subsonic wind tunnel. The test section in which the model is mounted is 2 m in width and 1.5 m in height. In the present study, the windspeed $U_\infty$ is set to 5.3 m/s and 32.5 m/s and the flow is characterised by a low level of turbulence (longitudinal free-stream turbulence intensity < 0.2%).

The experimental model, shown in Fig. 2, is the same as the one used by Dubois and Andrianne (2022). For the sake of completeness, the main features are reminded here. It consists in static cylinders with an external diameter $D$ of 0.125 m clamped on both sides using end-plates to minimise the three-dimensional effects. The aspect ratio

**Figure 2:** Picture of the experimental model installed in the aeronautical section of the wind tunnel of ULiège.

and a geometric blockage ratio are equal to 10 and 6.25%, respectively. The value of the blockage ratio is lower than 10%. Thus, no wall interference correction is applied as it is common practice in similar wind tunnel tests. The tested Reynolds numbers, $\mathrm{Re} = U_\infty D/\nu$, are therefore 45k[1] and 275k. Each cylinder is composed of two parts: an instrumented central part obtained by means of a 3D printing technique which allows to control the surface roughness near the measurement locations and steel parts on the extremities covered by sandpapers. The same equivalent surface roughness is used on the two parts ($k/D = 7.2\times10^{-3}$). This particular use of surface roughness has been analysed and validated in Dubois and Andrianne (2022). It allows to reach the post-critical flow regime at lower Reynolds numbers, hence at $\mathrm{Re} = 275$k. The set-up is mounted vertically on a turn-table, allowing to adjust accurately the wind incidence $\alpha$ of the cylinders with respect to the incoming flow. The wind incidence is varied from 0° (tandem arrangement) to 10° in increment of 2°.

Both cylinders are instrumented by 48 pressure taps of 1 mm in inner diameter, equally spaced on an instrumented section at the mid-span. Unsteady pressure is measured during 60 seconds at a sampling frequency of 600 Hz using a pressure scanner (from Turbulent Flow Instrumentation Pty Ltd) with a range of ±2.7 kPa. Dynamic effects of the pressure lines are corrected using the analytical model by Bergh and Tijdeman (1965). The pressure coefficient $C_p$ is calculated using

$$C_p(\theta,t) = \frac{p(\theta,t) - p_\infty}{1/2\rho U_\infty^2} \tag{1}$$

where $p(\theta,t)$ is the cylinder surface pressure measured by the pressure scanner and $p_\infty$ is the static pressure measured at the free-stream reference. The free-stream conditions are monitored by a Pitot-static probe located at $x/D$=-4.96 and $y/D$=-2.64 (Fig. 2). It provides the dynamic pressure ($1/2\rho U_\infty^2$) and allows to extract the flow velocity $U_\infty$ in the wind tunnel. Note that the origin of the xy-coordinates is found in the centre of the turn-table (Fig. 1).

The time-dependent pressure component of the two-dimensional lift coefficient $c_l$ is obtained by integrating the surface pressure,

$$c_l(t) \quad = \quad \frac{1}{2}\int_0^{2\pi} C_p(\theta,t)\sin(\theta-\alpha)d\theta, \tag{2}$$

where $\theta$ is the angular position on the cylinder, as defined in Fig. 1. In the present work, $C_p'$ and $c_l'$ correspond to the standard deviation of the pressure and lift coefficients, respectively.

---

[1] k stands for "thousand".

## 3. Lift force coefficient

Fig. 3(a-b) shows the variation of the time-averaged lift coefficient of each cylinder with the wind incidence in the sub- and post-critical flow regimes. Sub-figures (c-f) also show the *Power Spectral Density* (*PSD*) of the fluctuating lift signal of each cylinder as a function of the wind incidence in both flow regimes. The fluctuating lift signals are initially normalised by their respective standard deviation to allow the comparison of the frequency content at different wind incidences. The dimensionless Strouhal number $St = fD/U_\infty$ is used as the frequency variable. It takes values in the range $0 < St < 1$ in the present analysis. The superimposed black lines with different markers correspond to the different peaks, which are not harmonic (the frequency of one peak is not an integer multiple of the other one), observed in the spectra. Within the tested range of wind incidences, three different flow behaviours can be identified in the sub- or post-critical flow regime.

The first behaviour is observed at low wind incidences (range I: $\alpha = 0° - 2°$). In both flow regimes, the time-averaged lift coefficient of each cylinder remains close to zero, as shown in Fig. 3(a-b). Nevertheless, it can be observed that the lift coefficient of the front cylinder becomes slightly negative while the one of the rear cylinder becomes positive when increasing the wind incidence. The two flow regimes differ in the frequency content of the lift signals. In the sub-critical flow regime, a strong peak is observed at $St \approx 0.14$. A second and weaker peak is also identified at an

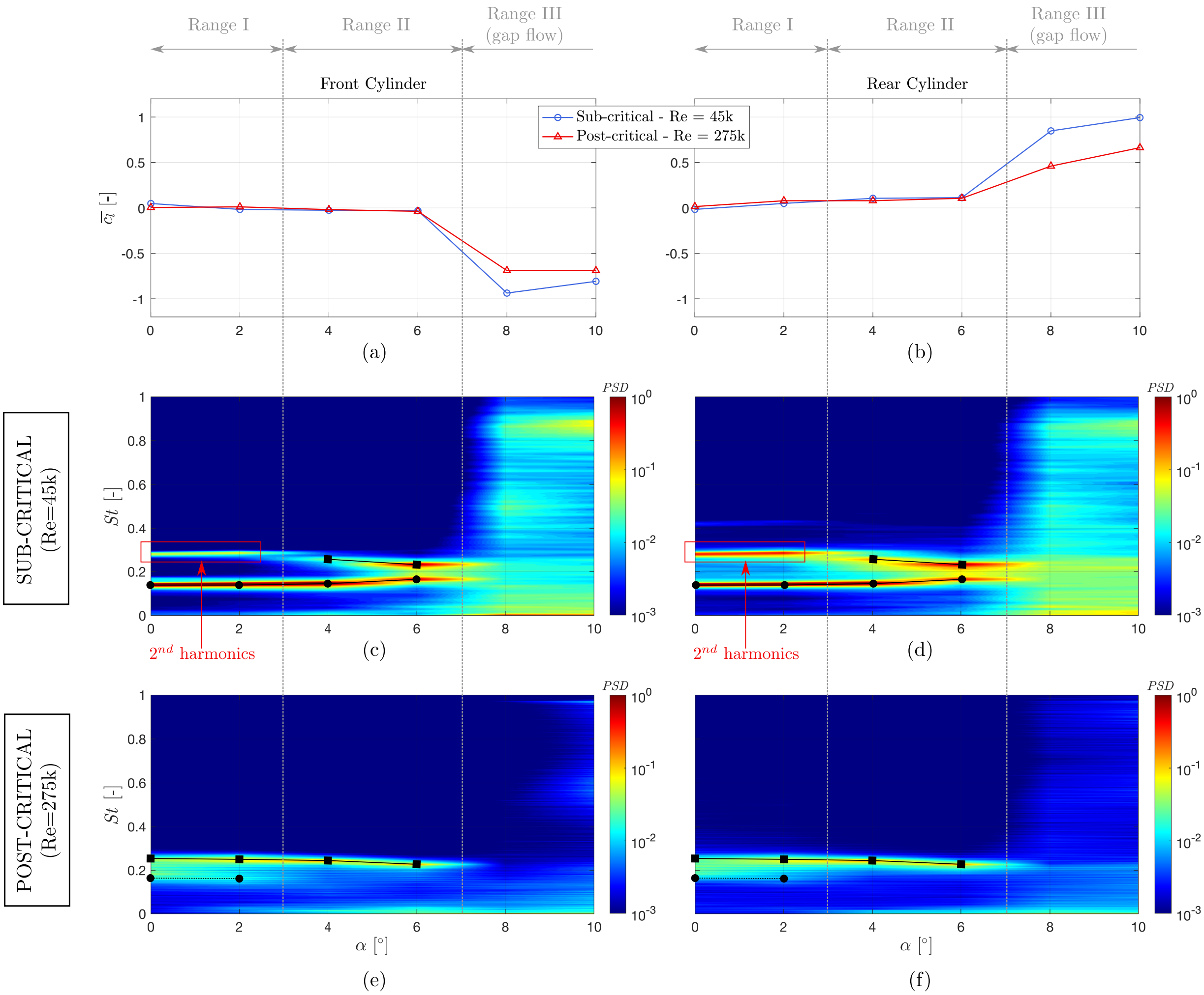

**Figure 3:** Variation of the time-averaged value and frequency content of the lift coefficient of each cylinder with the wind incidence in the sub- and post-critical flow regimes.

harmonic frequency of the fundamental one, $St \approx 0.28$ (see Fig. 3(c-d)). This observation was done by Dubois and Andrianne (2022) in the tandem configuration of cylinders ($\alpha = 0°$). The presence of harmonic components was attributed to the alternate re-attachment of the separated shear layers from the front cylinder onto the rear cylinder, as shown by Alam, Moriya, Takai and Sakamoto (2003). In the post-critical flow regime, the frequency content also reveals two peaks (see Fig. 3(e-f)). However, the second peak does not correspond to an harmonic component of the first one. This observation was done for the tandem configuration. Dubois and Andrianne (2022) concluded that it corresponds to a bi-stability due to the intermittent re-attachment of the separated shear layers from the front cylinder onto the rear cylinder.

A second behaviour is observed at intermediate wind incidences (range II: $\alpha = 4°$ - $6°$). Similarly to the low wind incidences, the lift coefficient of each cylinder remains small in both flow regimes. When increasing the wind incidence angle, the lift coefficient of the front cylinder slightly decreases and the one of the rear cylinder slightly increases. In the sub-critical flow regime, two peaks are still observed in the spectra of the lift signals (see Fig. 3(c-d)). Unlike the previous range of wind incidences, the peaks are identified at non-harmonic frequencies ($St \approx 0.14$ and 0.25). It is therefore assumed that they do emanate from two distinct processes. A bi-stability between two flow patterns takes place, leading to two different Strouhal numbers. The lowest identified Strouhal number increases when the wind incidence is increased from 4° to 6° while the other Strouhal number decreases. In the post-critical flow regime, a single peak is observed in the spectra at $St \approx 0.24$ (Fig. 3(e-f)). This peak corresponds to the highest Strouhal number identified in the previous sub-range of wind incidences. Thus, it is stated that only the eddy shedding process related to this Strouhal number is present in this configuration.

A third behaviour is observed at higher wind incidences (range III: $\alpha = 8°$ - $10°$). The time-averaged lift coefficients of the front and rear cylinders take large negative and positive values, respectively. The appearance of these large lift forces has already been observed in previous studies in the sub-critical flow regime (Zdravkovich (1987) or Sumner, Richards and Akosile (2005), among others) and is referred to the "inner" lift force. Those large lift forces are induced by a strong gap flow between the two cylinders. The gap flow occurs in the sub- and post-critical flow regime, as observed in Fig. 3(a-b). Based on the absolute values of the lift coefficients, it can be stated that the gap flow is stronger in the sub- than in the post-critical flow regime. The exact wind incidence angle at which the gap flow appears cannot be identified but it is expected between $\alpha = 6°$ and 8° for both flow regimes. Concerning the frequency content of the lift signals, it is observed that it is broadband within this range of wind incidences (see Fig. 3(c-f)). In both flow regimes, the occurrence of the broadband spectra coincides with the presence of a strong gap flow. Based on this observation, it can be stated that the gap flow strongly impacts the eddy shedding process behind the twin-cylinder configuration.

## 4. Case of bi-stability

In this section, the analysis focuses on the occurrence of a bi-stability, as previously observed in the frequency content of the lift forces. For this purpose, a methodology is proposed to extract the two stable states of the flow. The resulting flow modes are presented hereafter for a particular configuration, i.e. $\alpha = 4°$ in the sub-critical flow regime (Re = 45k). This particular configuration is chosen because the two modes are easily decoupled based on the observation of the lift signals, as it will be seen below, while it is not the case for the other flow regime and/or wind incidences. The proposed methodology will be then applied to the other flow regime and wind incidences.

### 4.1. Mode decomposition from lift signals

Fig. 4(a,c) shows typical time signals of the lift coefficient measured on the two cylinders. Additionally, their respective wavelet transforms are shown in Fig. 4(b,d). In the two different highlighted time intervals, it is observed that the lift coefficients do not fluctuate at the same frequency. Indeed, the lift coefficients do fluctuate at a lower frequency in the first highlighted time interval (Mode 1: $t \approx 49 - 53$ s) than in the second one (Mode 2: $t \approx 57.5 - 59.5$ s). This observation is corroborated by the variation of the wavelet transforms with time. In Fig. 4(b,d), it can be seen that modes 1 and 2 are associated with Strouhal numbers of 0.14 and 0.25, respectively.

The lift coefficients in each time interval highlighted in Fig. 4(a,c) (dashed boxes) are phase-averaged to ease the analysis of the modes. As it can be seen, the time interval corresponding to mode 1 is larger than the one corresponding to mode 2. This is done in order to have the same number of cycles in both modes (22 cycles here) when performing

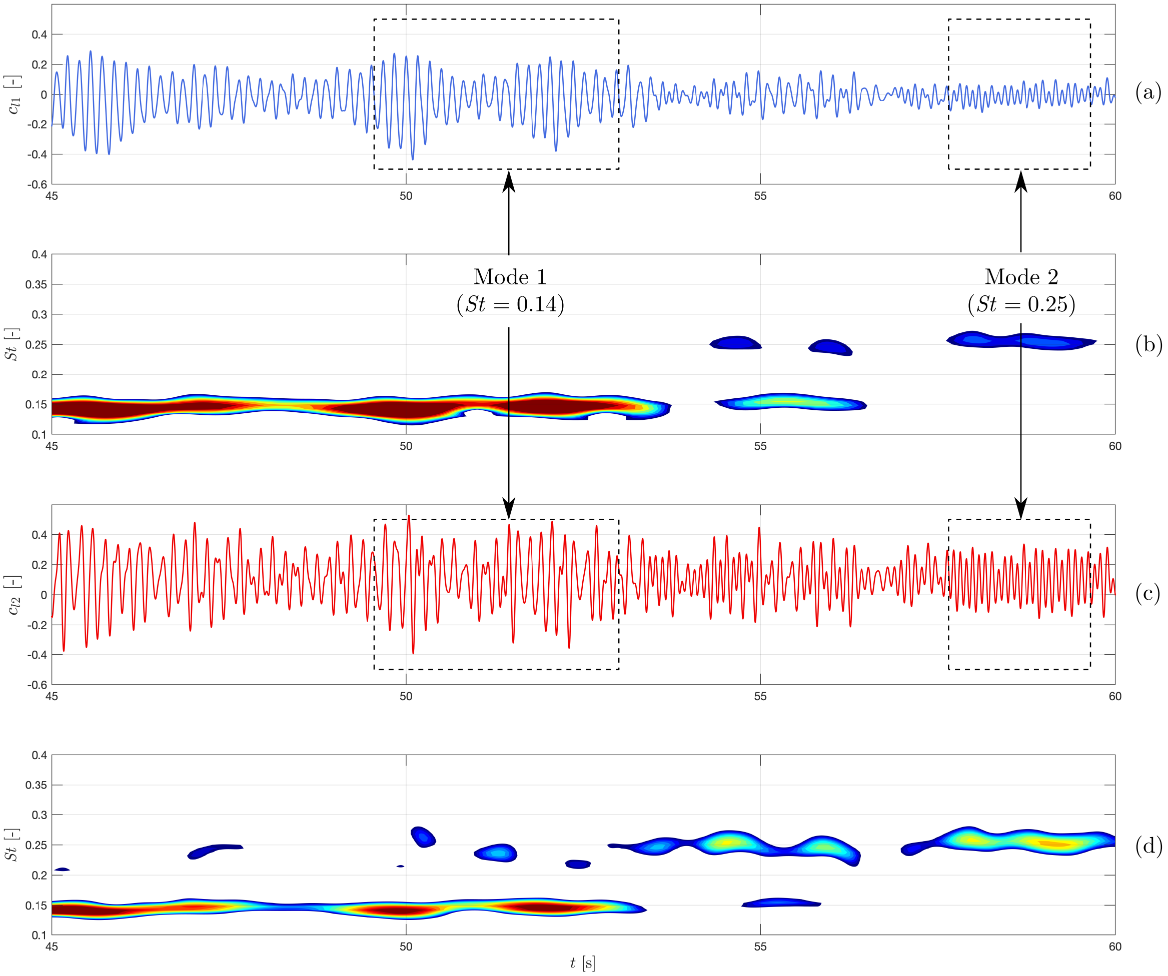

**Figure 4:** Time-frequency analysis of the lift coefficient of each cylinder: (a) signal $c_{l1}$, (b) wavelet norms of $c_{l1}$, (c) signal $c_{l2}$ and (d) wavelet norms of $c_{l2}$ (sub-critical: Re = 45k; $\alpha = 4°$).

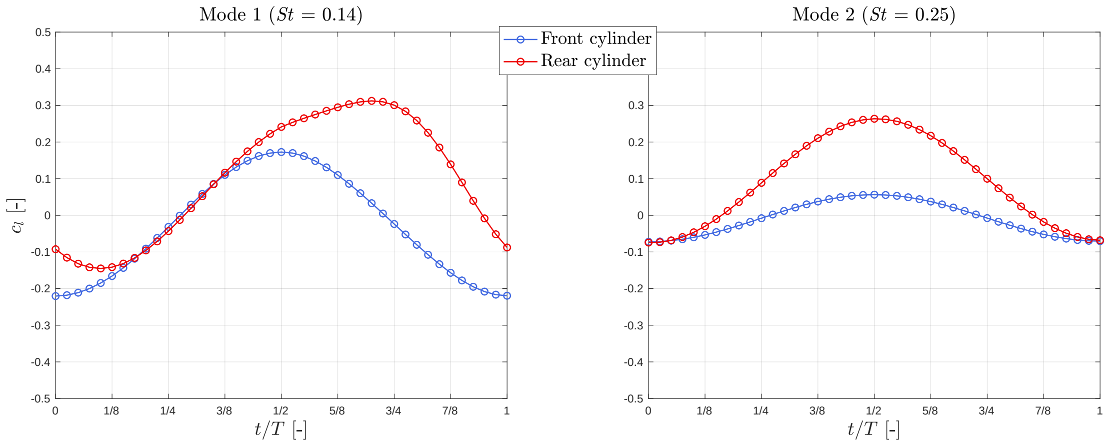

**Figure 5:** Phase-averaged lift coefficients of each cylinder in the identified modes for a particular configuration (sub-critical: Re = 45k; $\alpha = 4°$).

**Table 1**
Time-averaged and fluctuating lift coefficients of each mode computed from the phase-averaged lift coefficients shown in Fig. 5 (sub-critical: Re = 45k; $\alpha = 4°$).

| Mode | Cylinder | $\overline{c_l}$ | $c_l'$ |
|---|---|---|---|
| 1 | Front | -0.04 | 0.15 |
| | Rear | 0.10 | 0.17 |
| 2 | Front | -0.01 | 0.05 |
| | Rear | 0.09 | 0.12 |

the phase-averaging. The lift coefficient of the front cylinder is taken as the reference signal. It means that the different cycles within the time interval are separated by locating the minima of the lift coefficient of the front cylinder. The resulting cycles are averaged at 40 equally spaced time instants within the period. The resulting phase-averaged lift coefficient of each cylinder within the two modes is shown in Fig. 5.

The time-averaged and fluctuating values of the phase-averaged lift coefficients of each mode are summarised in Table 1. The lift force fluctuations are larger in the first mode than in the second one, especially for the front cylinder, while the time-averaged values do not change significantly. Another interesting observation is the phase-lag between the lift coefficients of the front and rear cylinders. In Fig. 5, it is observed that the lift force coefficients on both cylinders are in phase in the second mode ($St = 0.25$), while they are not in phase for the first mode. For mode 1, the lift signal of the rear cylinder is characterised by a second harmonic. Based on these observations, it can be stated that the fluctuating mechanisms of the two modes are not the same and correspond to two distinct flow patterns.

### 4.2. Phase-averaged pressure coefficients

The two modes are analysed in further details by means of the pressure coefficient distributions around the cylinders. To do so, the pressure coefficients are phase-averaged following the same procedure than previously done for the lift coefficients. Fig. 6 shows the variation of the phase-averaged pressure distribution on each cylinder within both modes. It is reminded that $\theta > 0°$ corresponds to the lower surface of the cylinder and $\theta < 0°$ to the upper surface (see Fig. 1). Fig. 7 also shows sketches of the flow modes to help the reader throughout the analysis and discussion.

The analysis first focuses on the pressure coefficient distributions at $t/T = 0$. For the front cylinder, a pressure coefficient equal to 1 is observed at $\theta \approx 4°$ in both modes (see Fig. 6). This maximum value in the pressure coefficient distribution corresponds to the stagnation point of the incoming flow on the front cylinder. From this particular point, the flow is divided into two parts. An upper and a lower boundary layers start developping. The flow accelerates in these regions before separating at $\theta \approx -67.5°$ and 75° from the upper and lower surfaces, respectively. The lower separated shear layer from the front cylinder re-attaches onto the rear cylinder (see Fig. 7). As a matter of fact, a local maximum value (which is characteristic of a re-attachment point) is observed in the pressure coefficient distribution of the rear cylinder at $\theta \approx 65°$ and 73° in modes 1 and 2, respectively. The corresponding maximum value is larger in mode 1 than in mode 2. Meanwhile, the upper separated shear layer from the front cylinder does not re-attach onto the rear cylinder (Fig. 7) because no local maximum value is identified on the upper surface of the rear cylinder in either mode (Fig. 6). The shear layer that re-attaches onto the lower surface of the rear cylinder also divides into two parts: a backward and forward boundary layers, as shown in Fig. 7. The flow accelerates in those parts leading to local minimum values in the pressure coefficient distribution on both sides of the re-attachment point, as observed in Fig. 6. In mode 1, the forward and backward boundary layers finally separate because of the adverse pressure gradients at $\theta \approx 15°$ and 120°, respectively. In mode 2, they respectively separate at $\theta \approx 22.5°$ and 120°. The forward separated shear layer from the rear cylinder finally re-attaches onto the back of the front cylinder (see Fig. 7). It leads to a local maximum value in the pressure coefficient distribution of the front cylinder at $\theta \approx 165°$ in mode 1 (see Fig. 6(a)) and 152.5° in mode 2 (see Fig. 6(b)). It can be noted that the latter local maximum value is more visible in mode 1 than in mode 2.

As $t/T$ increases within the shedding cycle of mode 1 (Fig. 6(a)), the local maximum value in the pressure coefficient distribution of the rear cylinder, which is associated with the re-attachment point, decreases. It is also observed that the corresponding angular location slightly moves downstream. At $t/T = 1/2$, it disappears along with the local minimum values on its both sides (Fig. 6(a)). Based on this observation, it is stated that the lower separated shear layer from the front cylinder does not re-attach anymore onto the rear cylinder at this time instant within the shedding cycle of mode 1 (see Fig. 7). The shear layer already re-attaches onto the lower surface of the rear cylinder at $t/T = 5/8$, as the local maximum value in the pressure coefficient distribution re-appears (see Fig. 6(a)). As $t/T$ increases, the re-attachment point moves upstream and the associated pressure coefficient increases again. This behaviour can be explained by the fact that the lower separated shear layer from the front cylinder moves downwards in the first half of the oscillation cycle and at some point does not re-attach onto the rear cylinder anymore. In the second half of the oscillation cycle, it moves upwards and re-attaches again onto the lower surface of the rear cylinder. There is an alternate re-attachment of the lower separated shear layer onto the rear cylinder. This statement is corroborated by the fact that the re-attachment of the forward separated shear layer from the rear cylinder onto the back of the front cylinder also disappears within the shedding cycle. Indeed, the local maximum value in the pressure coefficient at the back of the front cylinder cannot

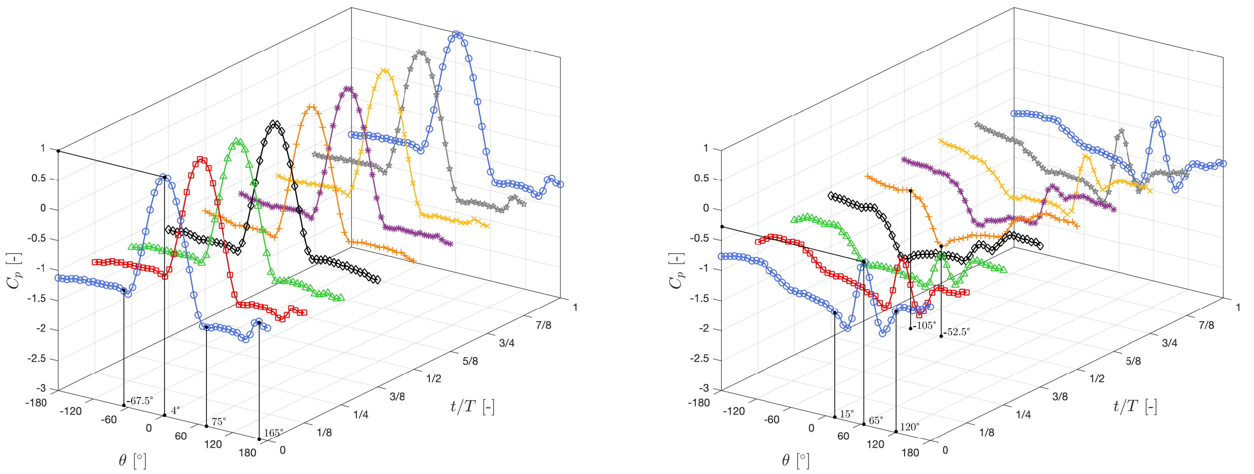

(a) Mode 1 - $St = 0.14$

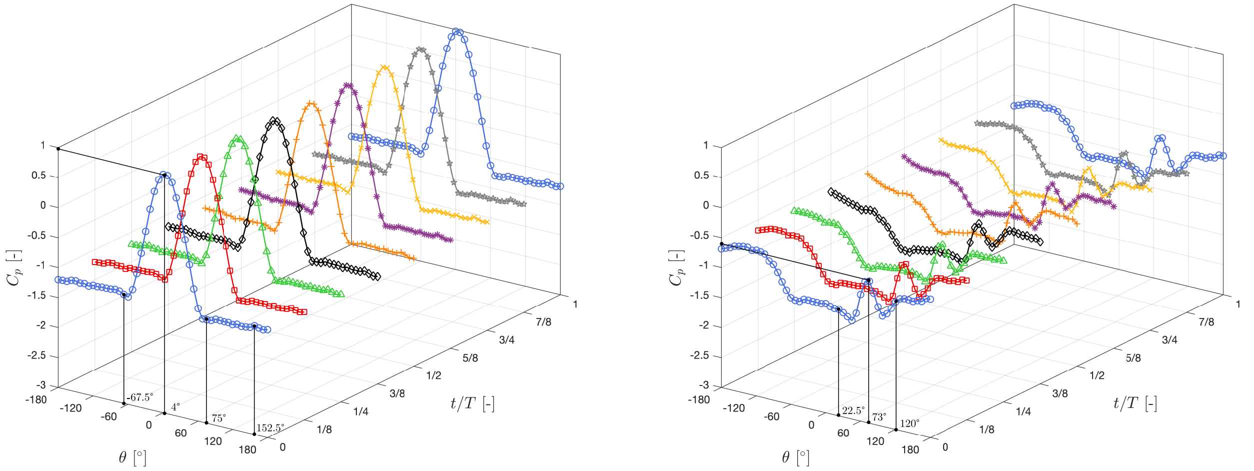

(b) Mode 2 - $St = 0.25$

**Figure 6:** Phase-averaged pressure coefficients around each cylinder in both modes (left: front cylinder; right: rear cylinder / sub-critical: Re = 45k; $\alpha = 4°$).

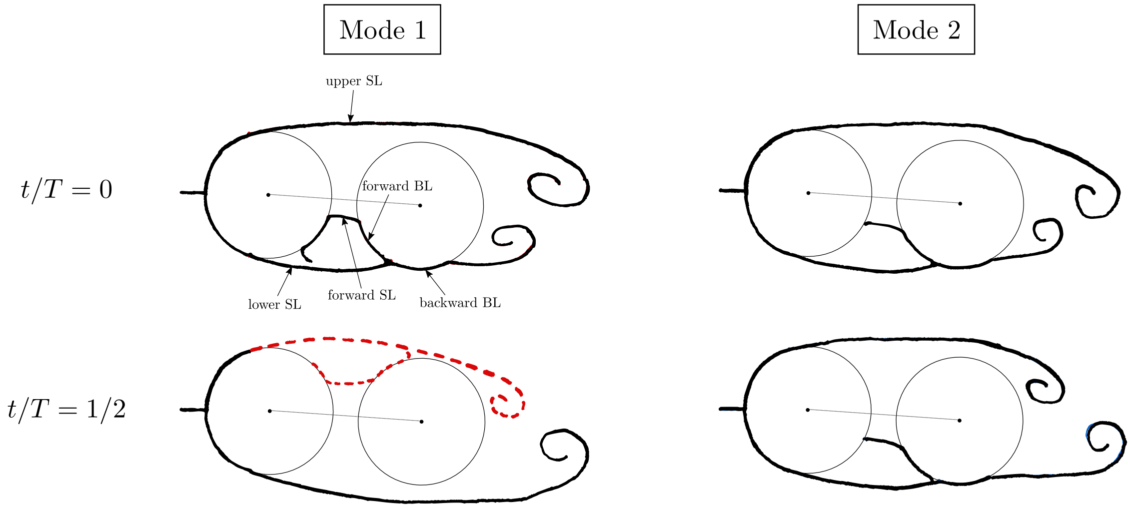

**Figure 7:** Flow sketches of the two modes: unclear behaviour in red dotted line (SL: shear layer; BL: boundary layer / sub-critical: Re = 45k; $\alpha = 4°$).

be observed when the lower separated shear layer from the front cylinder does not re-attach onto the rear cylinder (see Fig. 6(a)).
The analysis is more complex concerning the upper surfaces of the cylinders. It can be observed that a local minimum value in the pressure coefficient distribution of the rear cylinder appears at $\theta \approx -52.5°$ when $t/T$ increases in the first half of the shedding cycle. A very small local maximum value is also observed at $\theta \approx -105°$. A clear physical explanation cannot be provided and the upper shear layer is therefore drawn in red dotted in Fig. 7. Flow visualisation would be of great help in this case to identify the behaviour of the flow.

In mode 2 (Fig. 6(b)), the local maximum value in the pressure coefficient distribution of the rear cylinder ($\theta \approx 73°$) and the minimum values on both sides are always present within the entire shedding cycle. Moreover, their respective angular locations and values do not significantly vary. It is thus assumed that the lower separated shear layer from the front cylinder always re-attaches onto the rear cylinder in this mode and the re-attachment point only slightly moves within the shedding cycle (Fig. 7). It corresponds to a steady re-attachment of the lower separated shear layer from the front cylinder onto the rear cylinder. It is observed in Fig. 6(b) that the larger fluctuations of the pressure coefficient are located at the back of the rear cylinder ($|\theta| > 100°$). This observation will be more evident in the next section.

### 4.3. Extraction of modes from frequency contents

In this particular configuration (sub-critical flow regime: Re = 45k and $\alpha = 4°$), it was possible to decouple the two modes by selecting two different parts of the time signals. Unfortunately, it is not the case in the other configurations for which bi-stability is observed, as stated before. The objective of this section is therefore to present a new methodology allowing to extract and identify the modes based on the frequency content of the pressure coefficients.

Fig. 8 shows the spectra of the fluctuating pressure coefficients around each cylinder with a wind incidence of 4° in the sub-critical flow regime. The radial direction corresponds to the frequency variable, represented by the dimensionless Strouhal number, and the tangential direction refers to the angular location around the cylinders. It should be mentioned that the spectra are computed on the entire pressure signals, meaning that both modes intermittently take place within the signals. As a matter of fact, the two Strouhal numbers corresponding to the two modes are observed in Fig. 8. Second harmonic components of the Strouhal number associated with the first mode ($St = 0.14$) are also observable. The presence of these harmonic components is attributed to the alternate re-attachment of the separated shear layer from the front cylinder onto the rear cylinder, as it has already been stated before.

The amplitude of the *PSD* is associated with the energy distribution around each cylinder. This energy level is extracted at the Strouhal numbers corresponding to the two modes ($St = 0.14$ and $0.25$). This procedure aims at

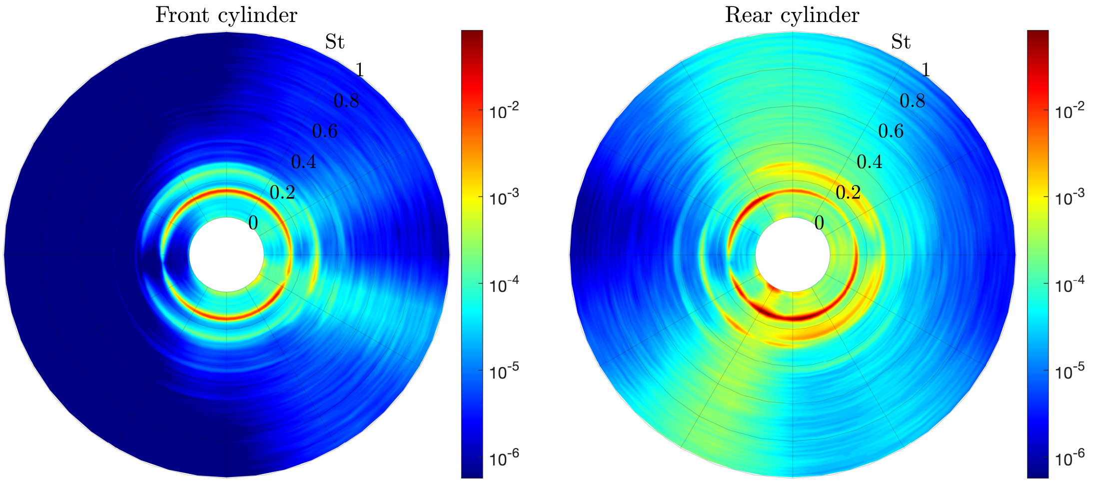

**Figure 8:** Frequency content of the pressure coefficients around each cylinder (sub-critical: Re = 45k; $\alpha = 4°$).

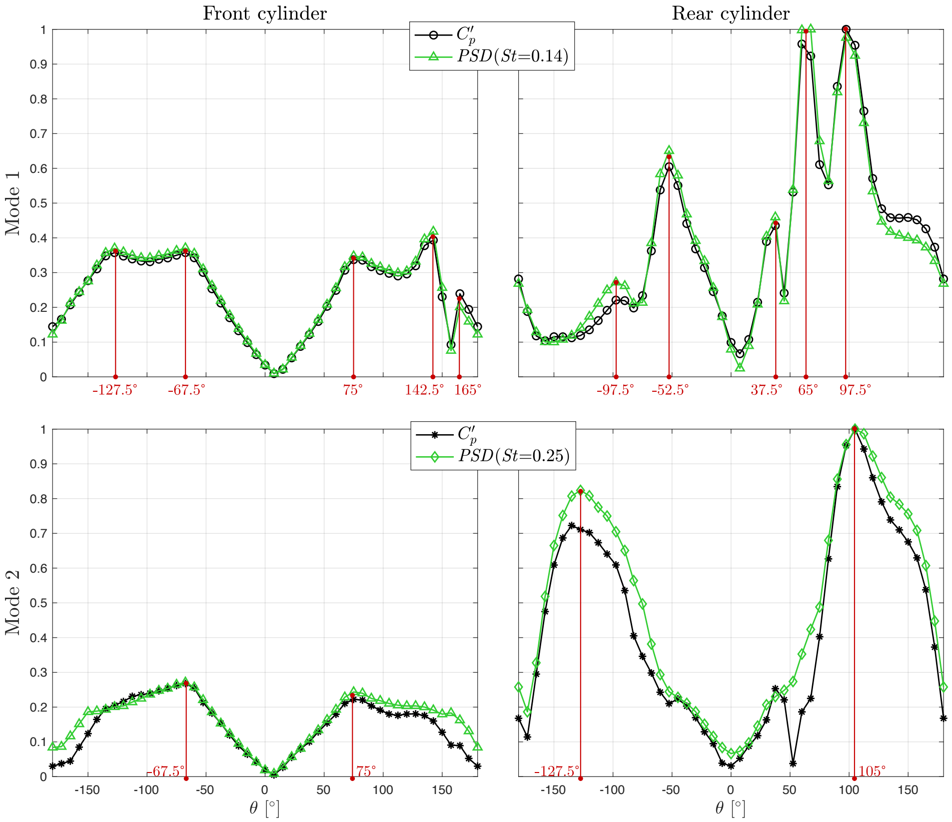

**Figure 9:** Extracted energy distributions of the pressure field of both modes (sub-critical: Re = 45k; $\alpha = 4°$).

giving an image of the fluctuating pressure coefficient distributions around the cylinders for a specific Strouhal number or equivalently, a specific mode. Fig. 9 shows these energy distributions associated with each mode extracted from the spectra of the pressure signals. Additionally, the fluctuating pressure distributions computed from the temporal pressure coefficients of each mode (highlighted time intervals in Fig. 4) are plotted for comparison . It should be pointed out that the different distributions are normalised by the maximum value of their respective fluctuating pressure distribution of the rear cylinder. It can be seen that the shape of the energy distributions compares very well with the fluctuating pressure distributions. Hence, it validates the statement made before: the energy distribution around the cylinders at specific Strouhal numbers shows an image of the fluctuating pressure distributions of the corresponding mode. The flow behaviour of each mode can be identified on the basis of the frequency content of the pressure fields.

In mode 1, three peaks are present on the lower surface of the rear cylinder ($\theta > 0°$). The peak at $\theta \approx 65°$ corresponds to the pressure fluctuations associated with the re-attachment point. The peaks on either sides of the re-attachment point ($\theta \approx 37.5°$ and $97.5°$) are induced by the appearance and disappearance of the backward and forward boundary layers because of the alternate re-attachment of the shear layer onto the rear cylinder (Fig. 7). The observation of these three peaks in the fluctuating pressure distribution of the rear cylinder has already been made by Alam et al. (2003) or Tsutsui (2012) in case of alternate re-attachment. On the upper surface of the same cylinder ($\theta < 0°$), two peaks can be identified. The largest one is located at $\theta \approx -52.5°$, where the local minimum value appears in the pressure coefficient distribution for $1/4 < t/T < 3/4$ (see Fig. 6(a)). The other peak is found at $\theta \approx -97.5°$. A clear physical explanation cannot be given here concerning those two peaks. Once again, it is stressed that flow visualisation would help to clarify the behaviour of the flow in this region. For the front cylinder, peaks are observed at $\theta \approx 75°$ and -67.5° in the fluctuating pressure distribution. Their location corresponds to the respective separation point of the boundary layer from the front cylinder. Two additional peaks are seen on the lower surface of the front cylinder at $\theta \approx 142.5°$ and 165°. It is assumed that the pressure fluctuations corresponding to those peaks are induced by the alternate re-attachment of the forward separated shear layer from the rear cylinder onto the back of the front cylinder (see Fig. 7). A local maximum value is also observed at $\theta \approx -127.5°$ on the upper surface of the front cylinder.

In mode 2, only two peaks are observed in the fluctuating pressure distribution of the rear cylinder. One is located on the lower surface at $\theta \approx 105°$ and the other one on the upper surface at $\theta \approx -127.5°$. Fluctuations are mostly observed at the back of the rear cylinder, as it was noticed earlier in Fig. 6(b). Those peaks are associated to the eddy shedding behind the rear cylinder (Fig. 7). Concerning the front cylinder, two maximum values are also observed at $\theta \approx 75°$ and -67.5° which correspond to the separation points on the lower and upper surfaces, respectively.

## 5. Effect of wind incidence and flow regime

The procedure presented above is applied to all the tested configurations for which no gap flow occurs between the cylinders ($\alpha < 8°$) in the sub- and post-critical flow regimes. Fig. 10 combines the time-averaged pressure distributions and the extracted modes for the different wind incidences in the sub-critical flow regime. In order to help the reader through the analysis and discussion, sketches of the identified flow patterns in the different wind incidence ranges and flow regimes are shown in Fig. 12.

In tandem configuration ($\alpha = 0°$), it is observed that the different distributions are rather symmetric. The slight asymmetry is attributed to a small misalignement of the cylinders with the incoming free-stream inside the wind tunnel. Only mode 1 is present in this configuration, i.e. no bi-stability is observed. It shows three peaks on either the lower or upper surface of the rear cylinder (see Fig. 10(d)). Based on the previous analysis, it is therefore stated that alternate re-attachment of the separated shear layers from the front cylinder occurs onto the lower and upper surfaces of the rear cylinder. The same conclusion has already been made in Dubois and Andrianne (2022). When the wind incidence is increased to 2°, the asymmetry switches side: the maximum fluctuating pressure is now located on the lower surface of the rear cylinder (see Fig. 10(d)). Three peaks of fluctuating pressures are still observed on either sides of the rear cylinder (see Fig. 10(d)), meaning that both separated shear layers from the front cylinder alternately re-attach onto the rear cylinder. Moreover, it can be assessed that the re-attachment of the upper separated shear layer is shorter and therefore weaker than the lower one, which leads to reduced fluctuating pressures. This analysis confirms the statement made before concerning the flow behaviour within this range of wind incidences: the separated shear layers from the front cylinder alternately re-attach onto the rear cylinder for $\alpha = 0°$ and 2° in the sub-critical flow regime and the associated Strouhal number is equal to 0.14. This flow pattern is sketched in Fig. 12(a).

The configuration with $\alpha = 4°$ has already been analysed and discussed in the previous section. Because of the presence of a bi-stability, two fluctuating modes can be extracted at $St = 0.14$ and $0.25$, respectively. In mode 1, the lower separated shear layer from the front cylinder alternately re-attaches onto the lower surface of the rear cylinder while the behaviour of the upper separated shear layer remains unexplained (red dotted line in Fig. 12(b)). In mode 2, the lower separated shear layer always re-attaches onto the rear cylinder. On the other hand, the upper separated shear layer does not re-attach and rolls up to form an eddy behind the rear cylinder. The large pressure fluctuations are mostly located at the back of the rear cylinder where eddies are shed. The corresponding flow pattern is sketched in Fig. 12(c). At $\alpha = 6°$, a bi-stability between two fluctuating modes also exists (see Fig. 3(c-d)) and the associated Strouhal numbers are 0.16 and 0.23. Mode 2, associated with $St = 0.23$, is very similar in shape in comparison to the second mode at $\alpha = 4°$ (see Fig. 10(e-f)). Based on this observation, it can be stated that the flow pattern is the same: the lower separated shear layer from the front cylinder always re-attaches onto the rear cylinder while the upper

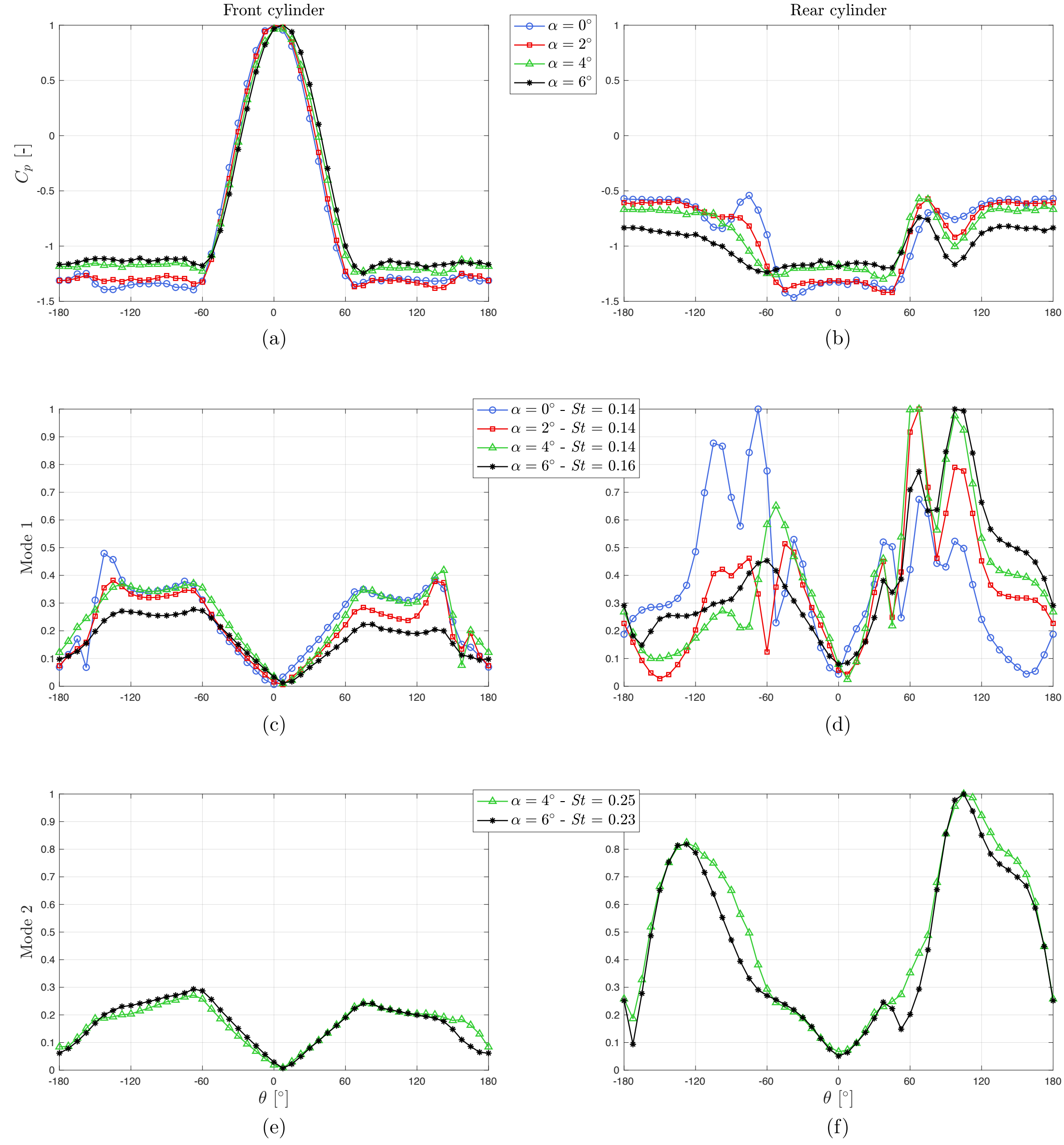

(a) (b)

(c) (d)

(e) (f)

**Figure 10:** Time-averaged pressure coefficients and fluctuating modes around each cylinder for different wind incidence angles in the sub-critical flow regime (Re = 45k).

shear layer does not re-attach and rolls up behind the rear cylinder where eddies are alternately shed from both sides (Fig. 12(c)). The decrease of the associated Strouhal number between $\alpha = 4°$ and $6°$ may be attributed to a widening of the wake due to the increase of the frontal area of the twin-cylinder configuration. Mode 1, associated with $St = 0.16$, is more difficult to analyse. Three peaks in the fluctuating pressures are still present on the lower surface of the rear cylinder. The larger peak is not associated with the re-attachment point anymore but to the backward boundary layer (see Fig. 10(d)). The peak on the upper surface of the same cylinder, observed at $\theta \approx -52.5°$ for $\alpha = 4°$, has slightly moved downstream to $\theta \approx -60°$ for $\alpha = 6°$.

Fig. 11 shows the time-averaged pressure distributions and the extracted modes for the different wind incidences in the post-critical flow regime. In this regime, mode 1 (associated to the low Strouhal number) only occurs for $\alpha = 0°$ and $2°$ since the bi-stability is observed in this range of wind incidences (see Fig. 3(e-f)). For the tandem configuration

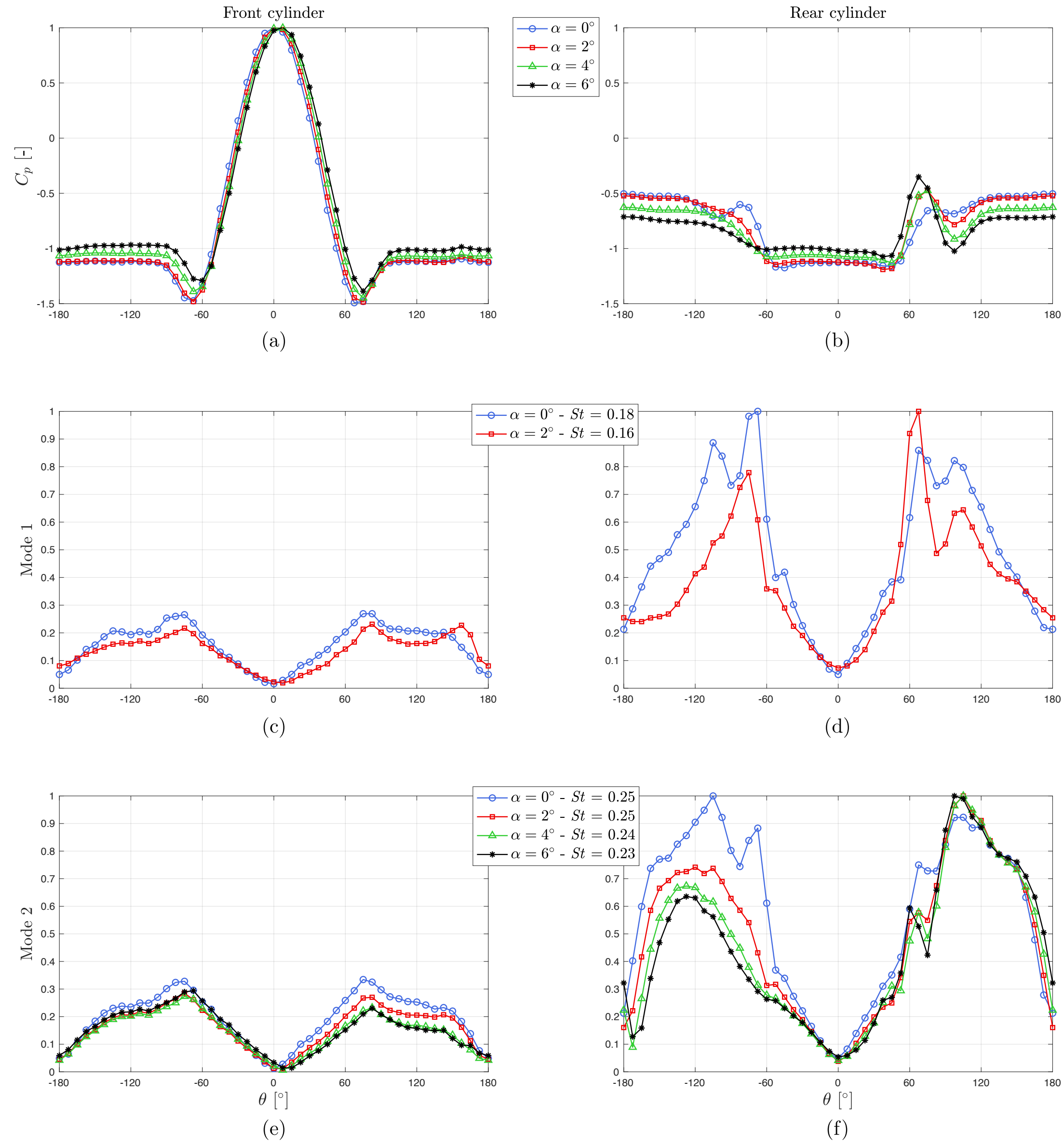

**Figure 11:** Time-averaged pressure coefficients and fluctuating modes around each cylinder for different wind incidence angles in the post-critical flow regime (Re = 275k).

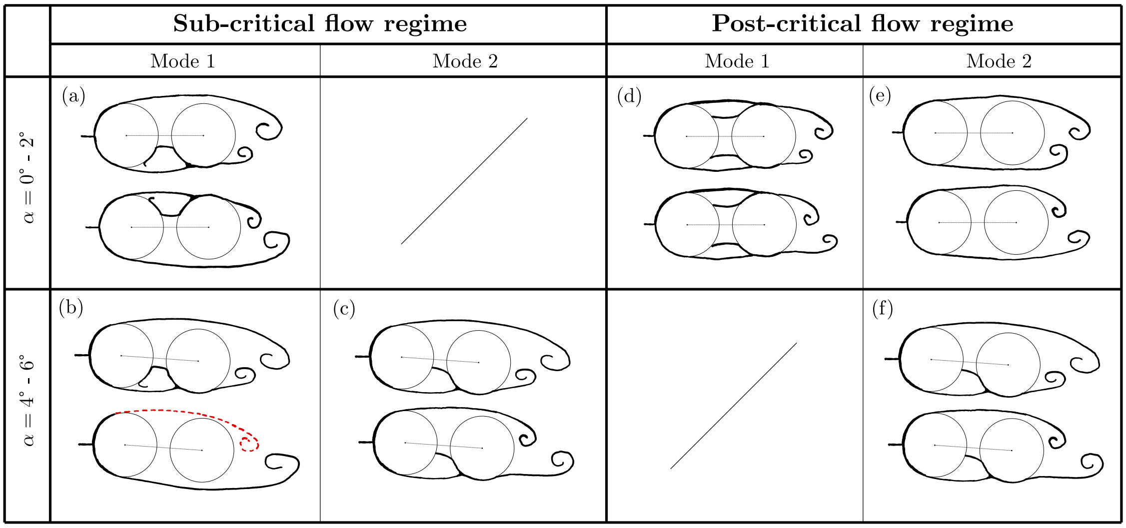

**Figure 12:** Sketches of the flow patterns identified at different wind incidences in the sub- and post-critical flow regimes: unclear behaviour in red dotted line.

($\alpha = 0°$), Dubois and Andrianne (2022) concluded that this fluctuating mode corresponds to the steady re-attachment of the separated shear layers from the front cylinder onto the rear cylinder (see Fig. 12(d)). Similarly, it is stated that the same flow behaviour occurs in this mode when the wind incidence is increased to 2° (see Fig. 11(c-d)).

The second mode (associated to the high Strouhal number) occurs for every wind incidences before the appearance of the gap flow, as shown in Figs. 3(e-f) and 11(e-f). For the tandem configuration, Dubois and Andrianne (2022) stated that this mode corresponds to the extended-body flow pattern, meaning that the separated shear layers do not re-attach onto the rear cylinder (Fig. 12(e)). This statement was based on the work about tandem cylinders made by Igarashi (1984). When the wind incidence increases, the lower separated shear layer does re-attach onto the rear cylinder (Fig. 12(f)) and the fluctuating pressure distributions of mode 2 are very similar to the ones of the second mode observed in the sub-critical flow regime (see Figs. 10(e-f) and 11(e-f)). The Strouhal number associated with mode 2 decreases with the wind incidence. Similarly to the sub-critical flow regime, this decrease may be explained by the widening of the wake due to the increase of the frontal area of the twin-cylinder configuration.

## 6. Gap flow

Fig. 13 shows the time-averaged pressure coefficients around each cylinder when the gap flow takes place for $\alpha = 8°$ and 10°. A sketch of the gap flow is also shown in Fig. 14 to ease the understanding of the analysis, once again. Note that the wake behaviour is not represented (e.g. no eddy) because a clear peak cannot be identified in the frequency content of the lift coefficients (Fig. 3(c-f)). The first observation concerns the difference in the pressure distributions between the sub- and post-critical flow regimes, especially in the gap between the cylinders.

In both flow regimes, a stagnation point can be identified on the lower surface of the rear cylinder ($C_p = 1$) at $\theta \approx 45°$ in Fig. 13(b,d). The flow divides into two parts at this stagnation point: a backward and forward boundary layers. The forward flow accelerates to large velocities, leading to lower pressure values. Depending on the wind incidence, the pressure coefficient reaches minimum value of -2.4/2.6 and -1.9/2.1 in the sub- and post-critical flow regimes, respectively. The minimum value is then followed by a large pressure recovery which leads to the separation of the boundary layer. The backward boundary layer also accelerates, but to a lesser extent, and then separates because of an adverse pressure gradient. It is observed that the pressure recovery before separation is larger in the post-critical flow regime than in the sub-critical one. The phenomenon is due to the difference in state of the boundary layer before separation: laminar and turbulent in the sub- and post-critical flow regime, respectively.

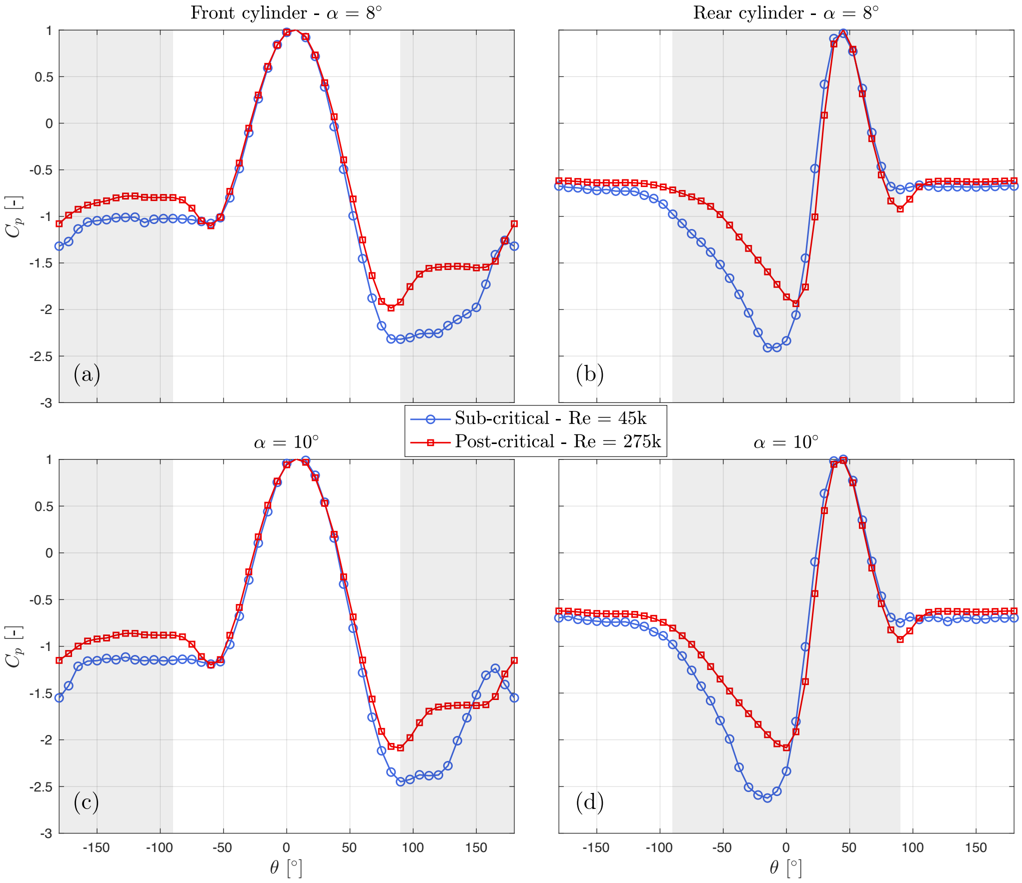

**Figure 13:** Time-averaged pressure coefficients around each cylinder with the occurrence of a gap flow ($\alpha = 8°$ and $10°$) in the sub- and post-critical flow regimes (grey zones: back and front faces of the front and rear cylinders, respectively).

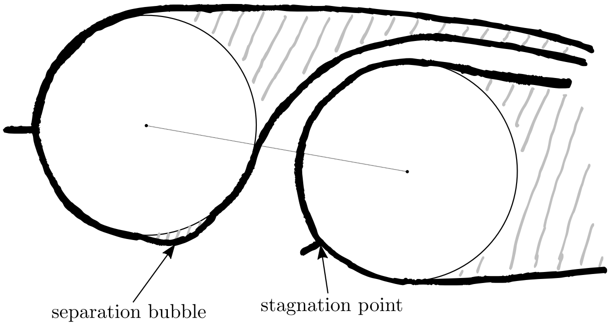

**Figure 14:** Sketch of the gap flow between the two cylinders.

The upper boundary layer on the front cylinder separates at $\theta \approx -67.5°$ and -75° in the sub- and post-critical flow regime, respectively. In the sub-critical flow regime, the lower boundary layer seems to first separate at $\theta \approx 100°$, followed by a small plateau in the pressure coefficient distribution (see Fig. 13(a,c)). This small plateau is characteristic of a separation bubble: the separated shear layer re-attaches onto the surface of the front cylinder. However, the exact angular location associated to this re-attachment is difficult to identify. It is followed by a pressure recovery up to $\theta \approx 172.5°$ or $165°$, either the wind incidence is $8°$ or $10°$. After this particular angular location, the flow accelerates as the pressure coefficient decreases up to $\theta \approx 180°$ and then it eventually separates from the surface of the front cylinder after another pressure recovery. In the post-critical flow regime, a plateau in the pressure coefficient distribution is also observed following the separation of the lower boundary layer from the front cylinder. This plateau is large in comparison with the one observed in the sub-critical flow regime. If there is a re-attachment of the separated shear layer onto the front cylinder, it is expected that the resulting separation bubble is larger than in the sub-critical flow regime. The plateau is then followed by a second pressure recovery.

## 7. Conclusions

The unsteady flow around twin rough cylinders is experimentally investigated in the sub- and post-critical flow regimes. The cylinders are set in close proximity ($L/D = 1.2$) and the wind incidence is varied from 0° up to 10°. The wind tunnel test campaign is performed in low turbulence flow conditions.

Three different flow behaviours can be identified in both flow regimes:

- At low wind incidences ($\alpha = 0°$ and $2°$):
    - In the sub-critical flow regime, the separated shear layers from the front cylinder alternately re-attach onto the rear cylinder. The associated Strouhal number is equal to 0.14. Moreover, second harmonic components are identified in the frequency contents of the lift signals.
    - In the post-critical flow regime, the separated shear layers from the front cylinder intermittently re-attach onto the rear cylinder. This bi-stable state leads to the existence of two distinct Strouhal numbers. The re-attachment pattern is associated to $St \approx 0.16 - 0.18$ and the extended-body pattern to $St \approx 0.25$.
    - In both flow regimes, the time-averaged lift coefficients remain very small.
- At intermediate wind incidences ($\alpha = 4°$ and $6°$):
    - In the sub-critical flow regime, the lower separated shear layer either alternately or steadily re-attaches onto the rear cylinder. Mode 1 corresponds to the alternate re-attachment and the associated Strouhal number is $0.14 - 0.16$. Mode 2 is associated to the steady re-attachment with $St \approx 0.23 - 0.25$. The behaviour of the upper separated shear layer remains unexplained in mode 1 but it can be stated that it does not re-attach onto the rear cylinder in mode 2.
    - In the post-critical flow regime, the lower separated shear layer from the front cylinder always re-attach onto the rear cylinder while the upper shear layer does not. The associated Strouhal number is $0.23 - 0.24$.
- At high wind incidences ($\alpha = 8°$ and $10°$):
    - In both flow regimes, the lift coefficient of each cylinder takes large non-zero values. The lift coefficient of the front cylinder is highly negative and the one of the rear cylinder positive. These large lift forces are generated by a strong gap flow between the cylinders.
    - The frequency contents of the lift coefficients become broadband with the appearance of the gap flow. Thus, it is stated that the gap flow strongly impacts the eddy shedding process behind the twin-cylinder configuration.
    - The lift forces being larger in the sub- than in the post-critical flow regime, it is assessed that the gap flow is stronger in the sub-critical flow regime. The analysis of the time-averaged pressure distributions around the cylinders reveals that the flow topology is not the same whether it is in the sub- or post-critical flow regime.

The conclusions are supported by an original method based on the analysis of the pressure measurements in the frequency domain. The resulting modes enable to identify important features of the flow behaviour around the cylinders.

## References

Alam, M.M., 2014. The aerodynamics of a cylinder submerged in the wake of another. Journal of Fluids and Structures 51, 393–400.

Alam, M.M., Moriya, M., Takai, K., Sakamoto, H., 2003. Fluctuating fluid forces acting on two circular cylinders in a tandem arrangement at a subcritical reynolds number. Journal of Wind Engineering and Industrial Aerodynamics 91, 139–154. doi:`https://doi.org/10.1016/S0167-6105(02)00341-0`.

Alam, M.M., Rastan, M., Wang, L., Zhou, Y., 2022. Flows around two nonparallel tandem circular cylinders. Journal of Wind Engineering and Industrial Aerodynamics 220, 104870.

Alam, M.M., Sakamoto, H., Zhou, Y., 2005. Determination of flow configurations and fluid forces acting on two staggered circular cylinders of equal diameter in cross-flow. Journal of Fluids and Structures 21, 363–394.

Bearman, P.W., Wadcock, A.J., 1973. The interaction between a pair of circular cylinders normal to a stream. Journal of Fluid Mechanics 61, 499–511. doi:`10.1017/S0022112073000832`.

Bergh, H., Tijdeman, H., 1965. Theoretical and experimental results for the dynamic response of pressure measurement systems. National Aero-and Astronautical Research Institute (Netherlands), Report NLR-TR F 238.

Dubois, R., Andrianne, T., 2022. Flow around tandem rough cylinders: Effects of spacing and flow regimes. Journal of Fluids and Structures 109, 103465.

Igarashi, T., 1981. Characteristics of the flow around two circular cylinders arranged in tandem: 1st report. Bulletin of JSME 24, 323–331. doi:`https://doi.org/10.1299/jsme1958.24.323`.

Igarashi, T., 1982. Characteristics of a flow around two circular cylinders of different diameters arranged in tandem. Bulletin of JSME 25, 349–357.

Igarashi, T., 1984. Characteristics of the flow around two circular cylinders arranged in tandem: 2nd report, unique phenomenon at small spacing. Bulletin of JSME 27, 2380–2387.

Okajima, A., 1979. Flows around two tandem circular cylinders at very high reynolds numbers. Bulletin of JSME 22, 504–511. doi:`https://doi.org/10.1299/jsme1958.22.504`.

Schewe, G., Jacobs, M., 2019. Experiments on the flow around two tandem circular cylinders from sub-up to transcritical reynolds numbers. Journal of Fluids and Structures 88, 148–166. doi:`https://doi.org/10.1016/j.jfluidstructs.2019.05.001`.

Sumner, D., 2010. Two circular cylinders in cross-flow: a review. Journal of Fluids and Structures 26, 849–899. doi:`https://doi.org/10.1016/j.jfluidstructs.2010.07.001`.

Sumner, D., Price, S.J., Païdoussis, M.P., 2000. Flow-pattern identification for two staggered circular cylinders in cross-flow. Journal of Fluid Mechanics 411, 263–303. doi:`10.1017/S0022112099008137`.

Sumner, D., Richards, M., Akosile, O., 2005. Two staggered circular cylinders of equal diameter in cross-flow. Journal of Fluids and Structures 20, 255–276.

Sun, T., Gu, Z., He, D., Zhang, L., 1992. Fluctuating pressure on two circular cylinders at high reynolds numbers. Journal of Wind Engineering and Industrial Aerodynamics 41, 577–588. doi:`https://doi.org/10.1016/0167-6105(92)90467-O`.

Tsutsui, T., 2012. Experimental study on the instantaneous fluid force acting on two circular cylinders closely arranged in tandem. Journal of wind engineering and industrial aerodynamics 109, 46–54.

Wang, L., Alam, M.M., Zhou, Y., 2018. Two tandem cylinders of different diameters in cross-flow: Effect of an upstream cylinder on wake dynamics. Journal of Fluid Mechanics 836, 5–42.

Younis, M., Alam, M., Zhou, Y., 2016. Flow around two non-parallel tandem cylinders. Physics of Fluids 28, 125106.

Zdravkovich, M.M., 1987. The effects of interference between circular cylinders in cross flow. Journal of Fluids and Structures 1, 239–261. doi:`https://doi.org/10.1016/S0889-9746(87)90355-0`.

Zdravkovich, M.M., 1997. Flow around circular cylinders, Volume 1: Fundamentals. Oxford University Press.

Zhou, Y., Feng, S., Alam, M.M., Bai, H., 2009. Reynolds number effect on the wake of two staggered cylinders. Physics of fluids 21, 125105.